Supporting Information

Table S1: Wyckoff positions, atomic coordinates, and equivalent isotropic displacement parameters U_{eq}/ Å^2 of the single-crystal determination (T = 183(2) K) of K_3MnF_6. U_{eq} is defined as one third of the trace of the orthogonalized U_{ij} tensor (standard deviations in parentheses).

Atom	Wyckoff position	*x*	*y*	*z*	U_{eq}
Mn1	8*d*	0	0	½	0.00649(3)
Mn2	8*c*	0	0	0	0.00605(3)
K1	16*f*	0.23093(2)	0.22648(2)	0.52404(2)	0.01103(4)
K2	16*f*	0.24170(2)	0.04249(2)	0.11161(2)	0.01171(4)
K3	8*e*	0	¼	0.36587(2)	0.01325(5)
K4	4*b*	0	¼	⅝	0.01357(7)
K5	4*a*	0	¼	⅛	0.01917(8)
F1	16*f*	0.01352(4)	0.01147(5)	0.11231(3)	0.01472(11)
F2	16*f*	0.08474(5)	0.07011(5)	0.58411(3)	0.01463(10)
F3	16*f*	0.09537(4)	0.05500(5)	0.42327(3)	0.01483(10)
F4	16*f*	0.14647(5)	0.14162(5)	0.24641(4)	0.01699(11)
F5	16*f*	0.37144(5)	0.13381(5)	0.23720(4)	0.01593(11)
F6	16*f*	0.41159(5)	0.13441(5)	0.01386(4)	0.01582(11)

Table S2: Anisotropic displacement parameters U_{ij} in Å^2 (standard deviations in parentheses) of the single-crystal determination at T = 183(2) K.

Atom	U_{11}	U_{22}	U_{33}	U_{23}	U_{13}	U_{12}
Mn1	0.00612(7)	0.00653(7)	0.00682(7)	0.00081(5)	0.00030(5)	0.00041(5)
Mn2	0.00568(7)	0.00673(7)	0.00574(6)	0.00030(5)	−0.00006(5)	0.00105(5)
K1	0.00993(7)	0.01167(8)	0.01148(7)	0.00175(6)	0.00153(6)	0.00255(5)
K2	0.01110(7)	0.01077(8)	0.01325(7)	−0.00181(6)	0.00013(6)	0.00146(6)
K3	0.01683(12)	0.01224(11)	0.01070(11)	0	0	−0.00303(9)
K4	0.00965(9)	0.00965(9)	0.02142(18)	0	0	0
K5	0.01706(11)	0.01706(11)	0.0234(2)	0	0	0
F1	0.0134(2)	0.0234(3)	0.0074(2)	−0.0025(19)	−0.00060(18)	−0.0007(2)
F2	0.0142(2)	0.0144(2)	0.0153(2)	0.0004(2)	−0.0019(2)	−0.00334(19)
F3	0.0134(2)	0.0165(3)	0.0146(2)	0.00034(2)	0.0050(2)	0.0003(2)
F4	0.0174(3)	0.0148(3)	0.0188(3)	−0.0022(2)	0.0030(2)	−0.0095(2)
F5	0.0156(3)	0.0147(2)	0.0174(3)	0.0028(2)	0.0042(2)	0.0068(2)
F6	0.0143(3)	0.0172(3)	0.0159(3)	0.0005(2)	−0.00139(19)	−0.0037(2)

Table S3: Interatomic distances in Å (standard deviations in parentheses) of the single-crystal determination (T = 183(2) K).

Mn1–F3	1.856(1)	2×	K1–F6	2.537(1)		K2–F2	2.594(1)		K3–F6	2.674(1)	2×
–F2	1.940(1)	2×	–F1	2.539(1)		–F3	2.699(1)		–F5	2.731(1)	2×
–F6	1.999(1)	2×	–F5	2.668(1)		–F5	2.748(1)		–F3	2.842(1)	2×
Ø	**1.932**		–F1	2.693(1)		–F1	2.763(1)		–F4	2.989(1)	2×
			–F2	2.764(1)		–F4	2.795(1)		–F1	3.233(1)	2×
Mn2–F4	1.851(1)	2×	–F3	2.768(1)		–F1	2.843(1)		**Ø**	**289.4**	
–F1	1.863(1)	2×	–F2	2.822(1)		–F5	2.849(1)				
–F5	2.086(1)	2×	–F3	3.168(1)		–F6	2.877(1)		K5–F1	2.957(1)	4×
Ø	**1.933**		**Ø**	**2.745**		–F4	3.092(1)		–F4	3.010(1)	4×
						Ø	**2.80.7**		–F5	3.119(1)	4×
K4–F2	2.546(1)	4×							**Ø**	**3.029**	
–F6	2.908(1)	4×									
Ø	**2.727**										

Table S4. Bond angles in deg (standard deviations in parentheses) of the single-crystal determination at T = 183(2) K.

F3–Mn1–F3	180	F3–Mn1–F2	91.09(3)	2×	F4–Mn2–F1	91.12(3)	2×
F2–Mn1–F2	180	F3–Mn1–F2	88.91(3)	2×	F4–Mn2–F1	88.88(3)	2×
F6–Mn1–F6	180	F3–Mn1–F6	87.99(2)	2×	F4–Mn2–F5	87.77(3)	2×
$Ø_{180}$	**180**	F3–Mn1–F6	92.01(3)	2×	F4–Mn2–F5	90.23(3)	2×
		F2–Mn1–F6	89.68(2)	2×	F1–Mn2–F5	89.09(2)	2×
F4–Mn2–F4	180.00(3)	F2–Mn1–F6	90.32(2)	2×	F1–Mn2–F5	90.92(2)	2×
F1–Mn2–F1	180	**$Ø_{90}$**	**90.00**		**$Ø_{90}$**	**89.67**	
F5–Mn2–F5	180.00(4)						
$Ø_{180}$	**180.00**						

Table S5: Charge distributions according to both the bond-valence sums (∑V) and the CHARDI (∑Q) concept.

	Mn1	Mn2	K1	K2	K3	K4	K5
∑V	+2.92	+2.98	+1.16	+1.05	+0.99	+1.23	+0.74
∑Q	+3.05	+2.85	+1.01	+1.01	+1.07	+1.00	+0.98

	F1	F2	F3	F4	F5	F6
∑V	–1.06	–1.12	–1.00	–0.89	–0.89	–0.96
∑Q	–1.09	–1.04	–1.00	–1.14	–0.83	–0.89

Table S6: Comparison of the calculated *MAPLE* values of K_3MnF_6 and the binary compounds KF ($Fm\bar{3}m$) and MnF_3 ($C2/c$).

Calculated MAPLE value for KF in kJ/mol	905	3×
Calculated MAPLE value for MnF_3 in kJ/mol	6437	
Calculated MAPLE value from the two educt compounds in kJ/mol	9151	
Calculated MAPLE value for K_3MnF_6 in kJ/mol	9209	
Deviation in %	0.6	

The *MAPLE* value (Madelung part of lattice energy) of K_3MnF_6 was calculated and compared to the sum of the *MAPLE* values of the binary compounds KF[1] and MnF_3[2]. The values are in good agreement with a deviation of 0.6%.

Table S7: Selected crystallographic data and details of the Rietveld refinement of K_3MnF_6.

Formula	K_3MnF_6
Molar mass / g·mol^{-1}	286.2
Space group (No.)	$I4_1/a$ (no. 88)
a / Å	12.37367(15)
c / Å	16.5748(2)
V / Å^3	2537.72(6)
Z	16
Pearson symbol	tI160
$\rho_{calc.}$ / g·cm^{-3}	2.9966
Color of the powder	Purple
T / K	293
λ / Å	1.54060 (Cu-$K_{\alpha 1}$)
$2\theta_{min}$, $2\theta_{max}$, $2\theta_{step}$ / °	3.885, 80.355, 0.015
No. of data points	5099
No. of parameters	53
No. of restrains	0
No. of constrains	0
Peak shape function	Pseudo-Voigt
Background	Manual
S	1.64
R_p, R_{wp} *	11.84, 8.90
$R_B(I)$	3.25
$\Delta\rho_{max}$, $\Delta\rho_{min}$ / e·Å^{-3}	0.35, −0.32

* Background-corrected R-factors

Table S8: Comparison of selected interatomic distances *d*, gained from single-crystal (*T* = 183(2) K) and powder data (*T* = 293(2) K), and their multiplicities *m* for the $[MnF_6]^{3-}$ octahedra.

Atom 1	Atom 2	*M*	d_{powder} / Å	$d_{single\text{-}crystal}$ / Å
Mn1	F2	2×	1.910(14)	1.940(1)
	F3	2×	1.842(14)	1.856(1)
	F6	2×	1.983(14)	1.999(1)
Mn2	F1	2×	1.851(9)	1.863(1)
	F4	2×	1.879(16)	1.851(1)
	F5	2×	2.068(15)	2.086(1)

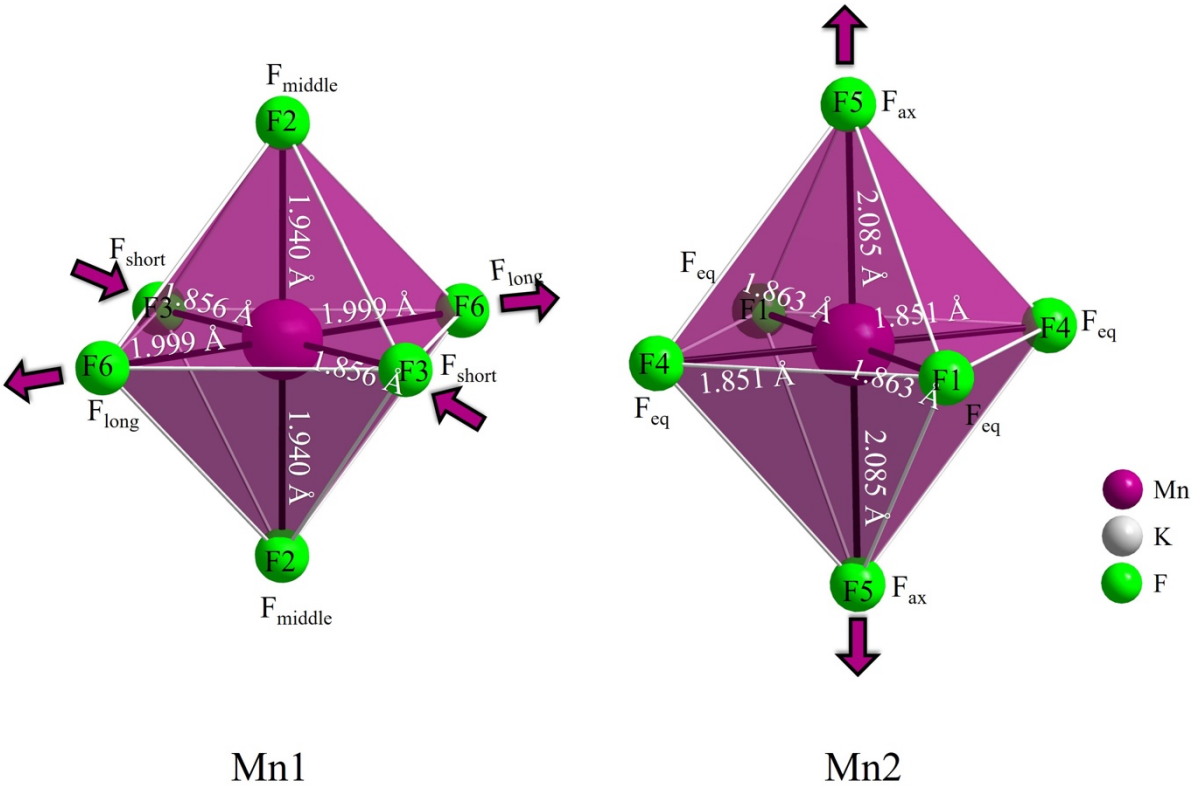

Figure S1: The two crystallographically different Mn atoms of $K_3[MnF_6]$ with distorted octahedral coordination spheres. The $[Mn(1)F_6]^{3-}$ anion is pseudo-rhombic while the $[Mn(2)F_6]^{3-}$ is pseudo-tetragonal with elongated axial Mn-F bonds. All atoms are numbered.

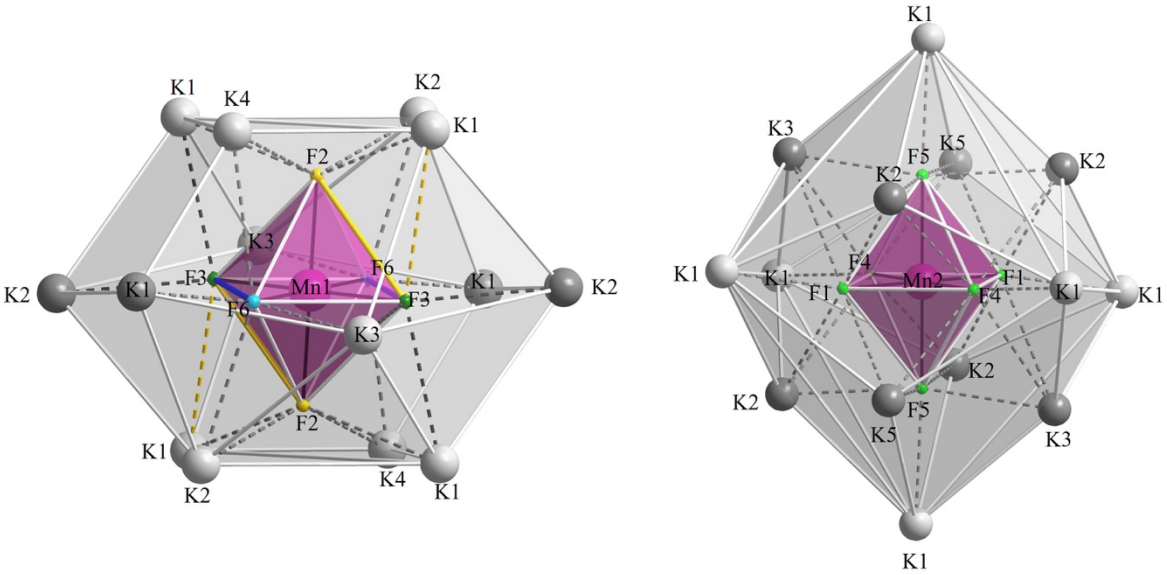

Figure S2: (left) Distorted tetrakis-hexahedral coordination sphere of pseudo-rhombic $[Mn(1)F_6]^{3-}$. The F3 sites are marked dark green. The large bond between F3 and K1 is indicated by a dashed and yellow colored line, signaling the 3+1 coordination of F3, which leads to the opening of the bridge at the yellow marked edges. Blue edges of the octahedra mark the two edges which are not bridged in a μ_2-manner by K^+ cations. Potassium cations drawn in a darker shade of gray represent the cations, which are just bound to one corner of the $[Mn(1)F_6]^{3-}$ anion. (right) Twofold-capped hexagonal prismatic coordination sphere of elongated $[Mn(2)F_6]^{3-}$. Hereby, the potassium cations of the second shell (cuboid) are drawn in a slightly darker gray than the ones of the third shell (octahedron). F atoms are pictured in green/yellow, manganese atoms in purple, and potassium atoms in grey. All atoms are numbered.

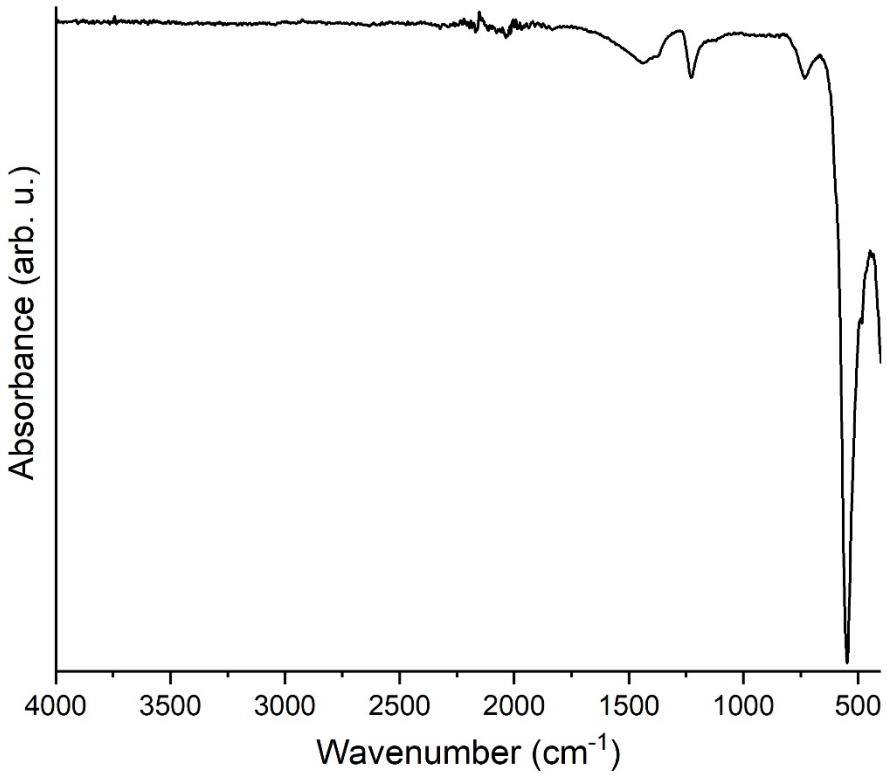

Figure 3: FT-IR spectrum of $K_3[MnF_6]$ in the range of 400 to 4000 cm^{-1}. experimentally obtained FT-IR spectrum of a powdered sample of $K_3[MnF_6]$. The sharp absorption band at around 550 cm^{-1} can be attributed to the $[MnF_6]^{3-}$ unit.[3] Additionally, there are some absorption bands with low intensity. One sharp band is located at about 730 cm^{-1}, likely belonging to small amounts of surplus starting material MnO_2.[4] Another sharp band at 1230 cm^{-1} and a broader one at around 1430 cm^{-1}, likely belong to KHF_2 (unreacted starting material).[5] In addition, there are no absorption bands visible above 1500 cm^{-1} and therefore, it is reasonable to exclude the presence of O–H bonds, hydroxide ions or H_2O molecules within the crystal structure.

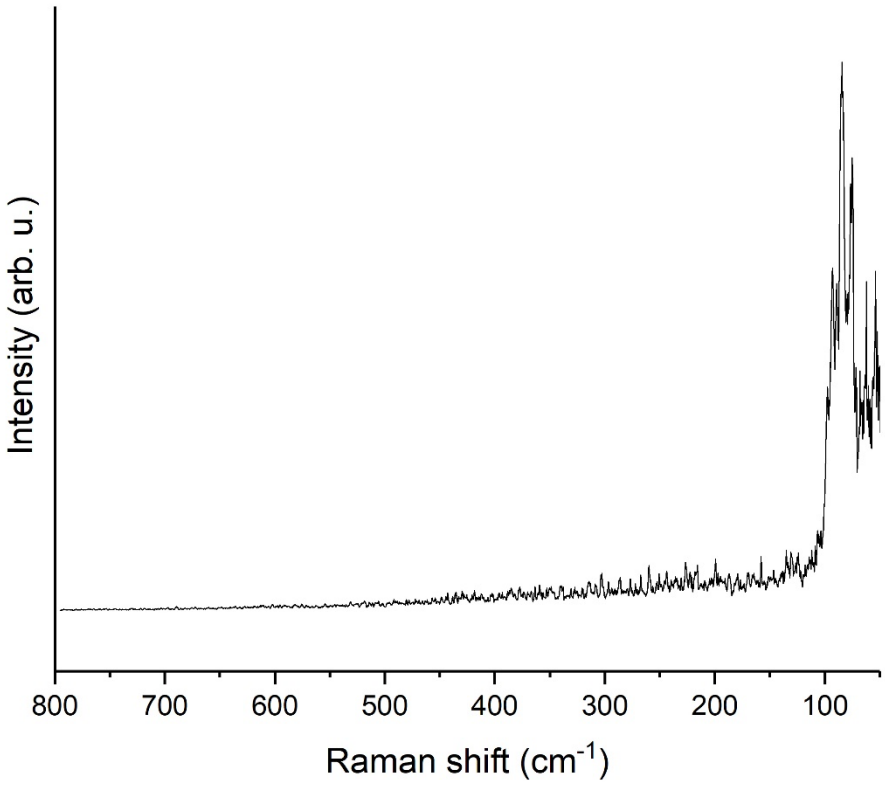

Figure S4: Raman spectrum of $K_3[MnF_6]$ in the range of 50 to 800 cm^{-1}.

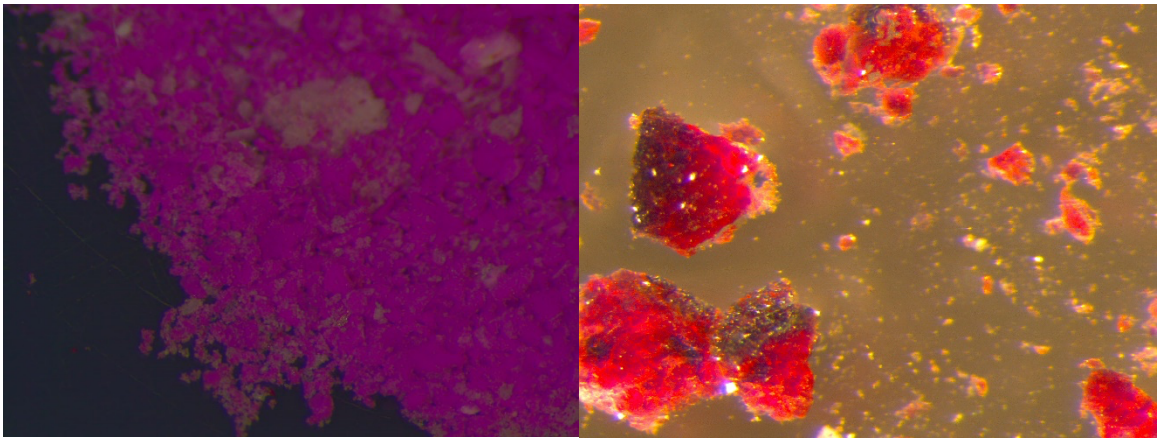

Figure S5: (left) Sample of $K_3[MnF_6]$, which shows a quite intense purple color, with some colorless impurities (K_2MnF_4), synthesized in a copper ampoule. (right) Crystals of $K_3[MnF_6]$, synthesized *via* a high-pressure/high-temperature approach, viewed through a polarization microscope.

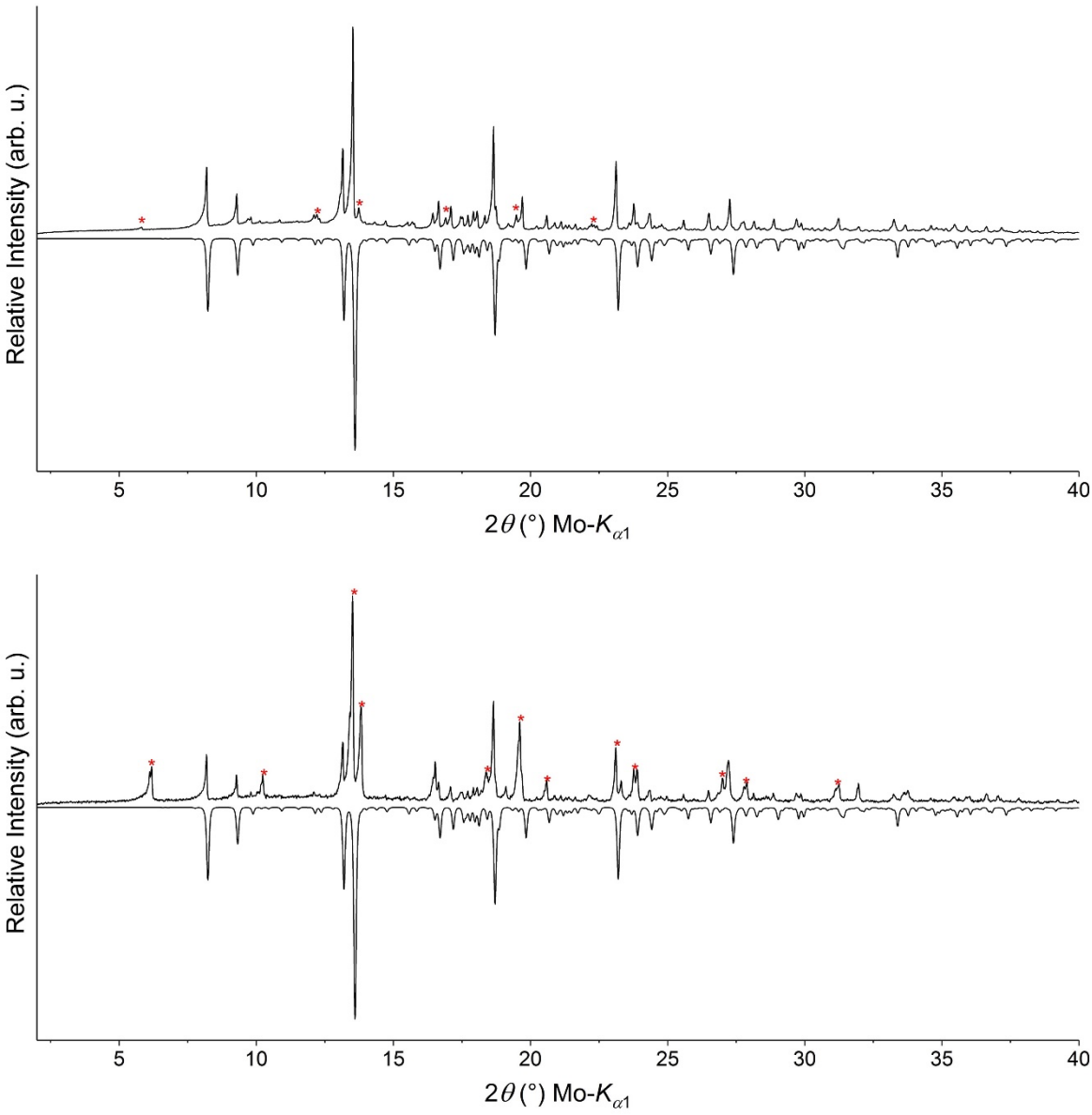

Figure S6: (top) Experimental powder pattern of the high-pressure/high-temperature experiment plotted against the theoretical powder pattern derived from single-crystal data. Reflections marked with a red asterisk stem from an unknown side product. (bottom) Experimental powder pattern of the high-temperature synthesis plotted against the theoretical powder pattern derived from single-crystal data. Reflections marked with a red asterisk stem from the side phase K_2MnF_4.

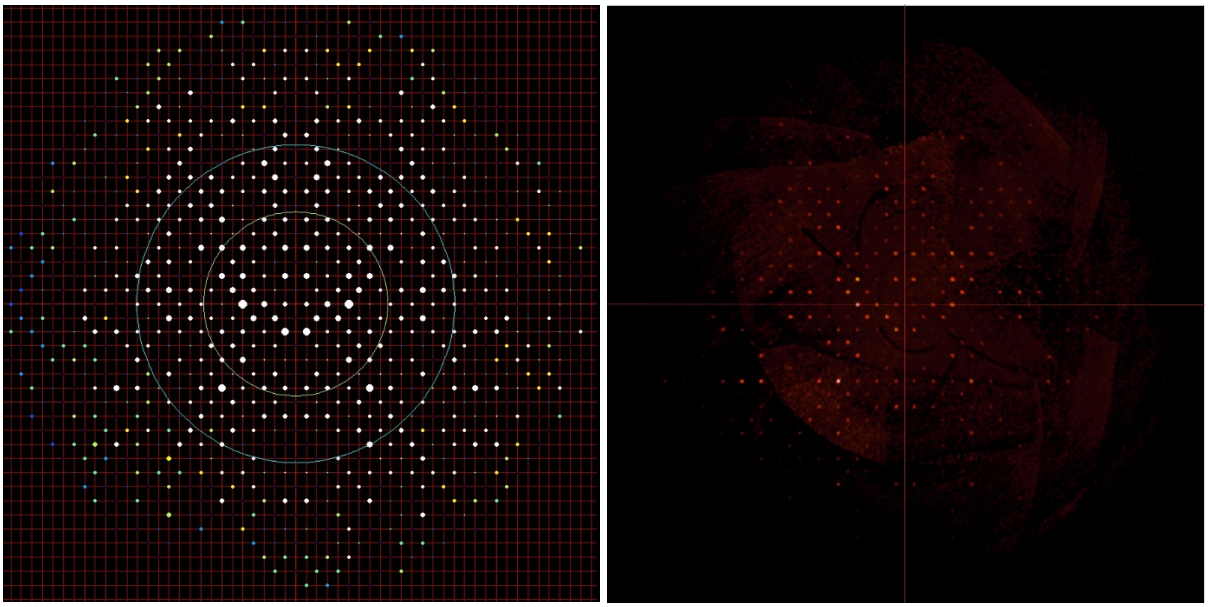

Figure S7: Simulated diffraction image of the 5*kl* layer (left) in comparison to the measured data of the 5*kl* layer (right). The extinction conditions ($h + k + l = 2n + 1$) for a body-centered cell apply.

Theoretical calculations

Angular overlap model analysis of the manganese-fluoride bonding:

The angular overlap model expressions of eq.1 was used assuming a dependence of the paramaters of σ and π-bonding $-e_\sigma$ and e_π on the Mn−F bond lengths R of $1/R^n$ with the power n taken as variable.

For the $[Mn(2)F_6]^{3-}$ site, eq.1 can be rewritten in the following form:

$$
\begin{aligned}
e(d_{xz}) &= 2e_\pi^o[(R_o / R_x)^n + (R_o / R_z)^n]; \\
e(d_{yz}) &= 2e_\pi^o[(R_o / R_y)^n + (R_o / R_z)^n]; \\
e(d_{xy}) &= 2e_\pi^o[(R_o / R_x)^n + (R_o / R_y)^n]; \\
e(d_{z2}) &= 2e_\sigma^o\{2(R_o / R_z)^n + (1/2)[(R_o / R_x)^n + (R_o / R_y)^n]\}; \\
e(d_{x2-y2}) &= (3/2)e_\sigma^o[(R_o / R_x)^n + (R_o / R_y)^n];
\end{aligned}
\qquad \text{(S1)}
$$

In eq.(S1), e_π^o and e_σ^o have been defined with respect to the average Mn−F bond length of the hypothetical regular $[MnF_6]^{3-}$ octahedron $R_o = (R_x + R_y + R_z)/2$, with R_x, R_y and R_z, the Mn−F bonds along the *x*, *y*, and *z* axes of the octahedron. The parameters e_π^o, e_σ^o, and *n* have been fitted to the ab-initio ligand field orbital energies, see Figure 13 (right) for their values.

In the case of the pseudo-rhombic $[Mn(1)F_6]^{3-}$ site, eqs.1 have been extended with an extra term:

$$\left\langle d_{z2} \left| V_{D2h} \right| d_{x2-y2} \right\rangle = -(\sqrt{3}/2)(e_\sigma^x - e_\sigma^y) \qquad \text{(S2)}$$

accounting for the mixing of the $3d_{z2}$ and $3d_{x2\text{-}y2}$ orbitals in the D_{2h} pseudo symmetry . This leads to a 2x2 off-diagonal block of the 5x5 ligand field matrix (orbital symmetry notations pertain to the D_{2h} pseudo symmetry of the ligand field: $d_{xy}(b_{1g})$, $d_{xz}(b_{2g})$, $d_{yz}(b_{3g})$; d_{z2} and $d_{x2\text{-}y2}$ (a_g)):

$$\begin{array}{ccccc} b_{1g} & b_{2g} & b_{3g} & a_g(d_{z2}) & a_g(d_{x2\text{-}y2}) \\ \left[\begin{array}{ccccc} e(d_{xy}) & 0 & 0 & 0 & 0 \\ 0 & e(d_{xz}) & 0 & 0 & 0 \\ 0 & 0 & e(d_{yz}) & 0 & 0 \\ 0 & 0 & 0 & e(d_{z2}) & \left\langle d_{z2} \left| V_{D2h} \right| d_{x2-y2} \right\rangle \\ 0 & 0 & 0 & \left\langle d_{z2} \left| V_{D2h} \right| d_{x2-y2} \right\rangle & e(d_{x2-y2}) \end{array}\right. & & & & \left.\begin{array}{c} \\ \\ \\ \\ \end{array}\right] \end{array} \qquad \text{(S3))}$$

From this analysis one gets for octahedral $[MnF_6]^{3-}$ (R_o = 1.933 Å): e_σ= 6255 cm^{-1}, e_π= 1630 cm^{-1}, n = 5.2 ($[Mn(1)F_6]^{3-}$) and e_σ= 5520 cm^{-1}, e_π= 1222 cm^{-1}, n = 6.7 (Mn(2)) reported and discussed in the text.

Jahn-Teller Effect in free $[MnF_6]^{3-}$ anions embedded in a conductor like polarizable water continuum

The coupling of the octahedral ^5E_g electronic ground state of the $[MnF_6]^{3-}$ anion to the $\varepsilon_g(Q_\theta,Q_\varepsilon)$ vibration (Figure 11) ($^5E_g \otimes \varepsilon_g$ –problem), up to second order vibronic coupling is described by the following Hamiltonian matrix $H_{^5E_g \otimes \varepsilon_g}$, adapted from the basic reference [6]:

$$\begin{array}{cc} \left|{}^5E_g,\theta\right\rangle & \left|{}^5E_g,\varepsilon\right\rangle \\ H_{^5E_g \otimes \varepsilon_g} = \left[\begin{array}{cc} (1/2)K_e(Q_\theta^2 - Q_\varepsilon^2) + A_1Q_\theta + A_2(Q_\theta^2 - Q_\varepsilon^2) & -A_1Q_\varepsilon + 2A_2Q_\theta Q_\varepsilon \\ -A_1Q_\varepsilon + 2A_2Q_\theta Q_\varepsilon & (1/2)K_\varepsilon(Q_\theta^2 - Q_\varepsilon^2) - A_1Q_\theta - A_2(Q_\theta^2 - Q_\varepsilon^2) \end{array}\right] \end{array} \qquad \text{(S4)}$$

The representation of the adiabatic Jahn-Teller Hamiltonian in the form of the matrix $H_{^5E_g \otimes \varepsilon_g}$ is done in the basis of the ^5E_g state using the rows of the standard irreducible representations – $\left|{}^5E_g, \theta\right\rangle$ and $\left|{}^5E_g, \varepsilon\right\rangle$ which correspong to the the $^5A_{1g}$ and $^5B_{1g}$ electronic ground states for the compressed and elongated geometries of D_{4h} symmetry, respectively. K_e, A_1 and A_2 are harmonic force constant, the linear and quadratic vibronic coupling constants, respectively. Restricting to the diagonal matrix elements, i.e. considering the $Q_\varepsilon = 0$ plane as a cross section along the 2D adiabatic potential energy surface the equation simplifies to:

$$E_\theta = (1/2)K_e(Q_\theta^2 - Q_\varepsilon^2) + A_1 Q_\theta + A_2(Q_\theta^2 - Q_\varepsilon^2) \quad \text{(S5)}$$

$$E_\varepsilon = (1/2)K_e(Q_\theta^2 - Q_\varepsilon^2) - A_1 Q_\theta - A_2(Q_\theta^2 - Q_\varepsilon^2) \quad \text{(S6)}$$

Minimization of eqs S5 and S6 leads to the following expressions for the stationary points – the elongation $Q_\theta^e > 0$ and the compression $Q_\theta^c > 0$along the θ and ε sheets of the potentail surface:

$$|Q_\theta^e| = \frac{A_1}{K_e - 2A_2} \quad \text{(S7)}$$

$$|Q_\theta^c| = \frac{A_1}{K_e + 2A_2} \quad \text{(S8)}$$

in which K_e, A_1 and A_2 are considered to be positive.

Using eqs. S5 and S6 we get the following expressions for the energies of the vertical (Franck-Condon) transitions from the ground to the excited split components of the ^5E_g ground state at the stationary points Q_θ^e and Q_θ^c:

$$E[\left|{}^5E, \theta\right\rangle \rightarrow \left|{}^5E, \varepsilon\right\rangle] = 2A_1\left|Q_\theta^c\right| + 2A_2\left|Q_\theta^c\right|^2 \quad \text{(S9)}$$

$$E[\left|{}^5E, \varepsilon\right\rangle \rightarrow \left|{}^5E, \theta\right\rangle] = 2A_1\left|Q_\theta^e\right| - 2A_2\left|Q_\theta^e\right|^2 \quad \text{(S10)}$$

Ignoring vibronic activity within the $^5T_{2g}$ excited state of octahedral $[MnF_6]^{3-}$ and denoting the harmonic force constant for the ε_g normal mode in this state by K_t one can write the energy of the vertical (Franck-Conon) transition from the stationary point of the lower sheet of the ^5E_g potential energy surface to the $^5T_{2g}$ excited state as

$$E[\left|{}^5E_g,\theta\right\rangle \rightarrow \left|{}^5T_{2g}\right\rangle] = \Delta + (1/2)(K_t - K_e)\left|Q_\theta^c\right|^2 + A_1\left|Q_\theta^c\right| - A_2\left|Q_\theta^c\right|^2 \quad \text{(S11)}$$

$$E[\left|{}^5E_g,\varepsilon\right\rangle \rightarrow \left|{}^5T_{2g}\right\rangle] = \Delta + (1/2)(K_t - K_e)\left|Q_\theta^e\right|^2 + A_1\left|Q_\theta^e\right| + A_2\left|Q_\theta^e\right|^2 \quad \text{(S12)}$$

Where by Δ we denote the 10Dq value of the undistorted $[MnF_6]^{3-}$ octahedron. DFT geometry optimizations yield values for $\left|Q_\theta^c\right|$ and $\left|Q_\theta^e\right|$, 0.225 and 0.316 Å, respectively. NEVPT2 calculations alow to extract the energie of d-d transitions at the stationary points:

Compressed:

$E[\left|{}^5E,\theta\right\rangle \rightarrow \left|{}^5E,\varepsilon\right\rangle]$: 5280 cm^{-1};

$E[\left|{}^5E_g,\theta\right\rangle \rightarrow \left|{}^5T_{2g}\right\rangle]$: 17050 (hole on d_{xz}), 17569 (hole on d_{yz}), 18627 (hole on d_{xy}), average energy 16973 cm^{-1};

Elongated:

$E[\left|{}^5E,\theta\right\rangle \rightarrow \left|{}^5E,\varepsilon\right\rangle]$: 9499 cm^{-1};

$E[\left|{}^5E_g,\theta\right\rangle \rightarrow \left|{}^5T_{2g}\right\rangle]$: 18543 (hole on d_{xy}), 20469 (hole on d_{yz}), 20709 (hole on d_{xz}), average energy 18454 cm^{-1};

Using eqs. S7-S12 a best fit to the data from the DFT and NEVPT2 calculations yields the model parameters:

A_1=15332 $cm^{-1}/Å$;

A_2=4516 $cm^{-1}/Å^2$;

K_e=58074 $cm^{-1}/Å^2$; (S13)

K_t=34231 $cm^{-1}/Å^2$;

Δ=14350 cm^{-1};

Standard deviation:511 cm^{-1}

Let us note softening of the harmonic potential energy surface when transfering one t_{2g} electron to the e_g orbital when exciting from ^5E_g to the $^5T_{2g}$ excited state.

The parameters A_1, A_2 and K_e have been used to plot the contour level diagram (Figure 12 top).

Vibronic Coupling Model for the compressed, orthorhombically distorted $[Mn(1)F_6]^{3-}$ and tetragonally elongated $[Mn(2)F_6]^{3-}$ octahedra in K_3MnF_6

In the local symmetry C_i of the $[Mn(1)F_6]^{3-}$ and $[Mn(2)F_6]^{3-}$ complexes in K_3MnF_6, the ^5E_g ground state of octahedral free $[MnF_6]^{3-}$ splits into two non-degenerate S = 2 states, $^5A_g(1)$ and $^5A_g(2)$. A vibronic analysis *must* start from a reference geometry for both $[Mn(1)F_6]^{3-}$ and $[Mn(2)F_6]^{3-}$ with equal bond distances, which can be approximated with the average of $[MnF_6]^{3-}$ bond lengths given by the structural data. These average distances are almost the same for the $[Mn(1)F_6]^{3-}$ and $[Mn(2)F_6]^{3-}$ anions. For this reason, contributions of the totally symmetric α_{1g} octahedral breathing mode to vibronic coupling are neglected. Because of influences of different surroundings of the $[Mn(1)F_6]^{3-}$ and $[Mn(2)F_6]^{3-}$ complex units dominated by the electrostatic field due to K^+ ions, the $^5A(1)[^5A_{1g}]$ and $^5A(2)[^5B_{1g}]$ states (D_{4h} point symmetry notations) will split in zero order. Let us denote their energies by $E_o(^5A_{1g})$ and $E_o(^5B_{1g})$, respectively. Periodic DFT calculations may be used to approximate these energies, as was convincingly demonstrated for Cu^{2+} doped tetragonal host lattices K_2ZnF_4 [7] and Ba_2ZnF_6.[8]

However, for K_3MnF_6 with Mn^{III} with four unpaired electrons, correlation effects requiring superposition of Slater determinants needed to describe the five S = 2 states of $[MnF_6]^{3-}$ could not be captured by single determinant DFT. Thus, while being very successful for solids including Cu^{2+} with a single hole in the d^9 configuration, periodic DFT calculations (see last part of the ESI) could not reproduce the local geometry of the compressed $[Mn(1)F_6]^{3-}$ site, which turned to be tetragonally elongated. For this reason, and for the sake of plotting ground state potential surfaces for $[Mn(1)F_6]^{3-}$ and $[Mn(2)F_6]^{3-}$ (Figure 12 middle and bottom, respectively), the vibronic coupling Hamiltonian H_{vibr} (eq. S14) with diagonal elements, eqs. S15, S16, and off-diagonal element eq. S17 can be used.

$$H_{vibr} = \begin{bmatrix} E(^5A_{1g}) & V_{12} \\ V_{12} & E(^5B_{1g}) \end{bmatrix} \qquad \text{(S14)}$$

diagonal elements:

$$E(^5A_{1g}) = E_o(^5A_{1g}) + A_\theta^1 Q_\theta + A_\varepsilon^1 Q_\varepsilon \qquad \text{(S15)}$$

$$E(^5B_{1g}) = E_o(^5B_{1g}) + A_\theta^2 Q_\theta + A_\varepsilon^2 Q_\varepsilon \qquad \text{(S16)}$$

Off-diagonal matrix element:

$$V_{12} = E_o^{12} + A_\theta^{12} Q_\theta + A_\varepsilon^{12} Q_\varepsilon \qquad \text{(S17)}$$

In the eqs. S15-S17, nuclear displacement Q_θ and Q_ε (Figure 11) become totally symmetric in the C_i site symmetry of $[Mn(1)F_6]^{3-}$ and $[Mn(2)F_6]^{3-}$. Focussing on the ground state only, neglecting the mixing term V_{12} and approximating the harmonic term $(1/2)(K_\theta Q_\theta^2 + K_\varepsilon Q_\varepsilon^2)$ in terms of single effective harmonic force constant K, $(1/2)K(Q_\theta^2 + Q_\varepsilon^2)$, we arrive at

eq. 3 of the main text, describing the adiabatic potential of a two dimensional harmonic oscillator shifted along the totally symmetric in C_i symmetry nuclear displacements Q_θ and Q_ε. We applied this simple model to the $[Mn(1)F_6]^{3-}$ and sites $[Mn(2)F_6]^{3-}$ separately and extracted values for the parameters *K*, A_θ and A_ε from the knowledge of the shifts along the coordinates Q_θ and Q_ε corresponding to the observed two structures - $Q_\theta^{rh} = 0.014$; $Q_\varepsilon^{rh} = 0.143$ Å (pseudo-rhombic (rh) site $[Mn(1)F_6]^{3-}$) and $Q_\theta^{tetr} = 0.265$; $Q_\varepsilon^{tetr} = 0.012$ Å (pseudo-tetragonal (tetr) site $[Mn(2)F_6]^{3-}$) and the vibronic stabilization energies E_{vibr} −1866 and −2434 cm^{-1}, computed using NEVPT2 state specific $[MnF_6]^{3-}$ cluster calculations for the $^5A_g(1)$ and $^5A_g(2)$ ground states of $[Mn(1)F_6]^{3-}$ and $[Mn(2)F_6]^{3-}$, respectively.

$$E = (1/2)K\ (Q_\theta^2 + Q_\varepsilon^2) + A_\theta Q_\theta + A_\varepsilon Q_\varepsilon \qquad \text{(S18)}$$

Minimizing the energy E with respect to Q_θ and Q_ε than yields:

$$Q_\theta^{tetr(rh)} = -A_\theta^{tetr(rh)} / K \qquad \text{(S19)}$$

and

$$Q_\varepsilon^{tetr(rh)} = -A_\varepsilon^{tetr(rh)} / K \qquad \text{(S20)}$$

from which we get

$$E_{stab}^{e(c)} = -(1/2)A_{\theta}^{e(c)2} / K - (1/2)A_{\varepsilon}^{e(c)2} / K = -(1/2)K(Q_{\theta}^{e(c)2} + Q_{\varepsilon}^{e(c)2}) \quad \text{(S21)}$$

and therefore:

$$K = 2E_{stab}^{e(c)} / = (Q_{\theta}^{e(c)2} + Q_{\varepsilon}^{e(c)2}) \text{(S22)}$$

$$A_{\theta}^{tetr(rh)} = -KQ_{\theta}^{tetr(rh)} \quad \text{(S23)}$$

$$A_{\varepsilon}^{tetr(rh)} = -KQ_{\varepsilon}^{tetr(rh)} \quad \text{(S24)}$$

Substituting the values of Q_{θ} and Q_{ε} and E_{JT} into the set of eqs. (S22)-(S24) values of K, A_{θ} and A_{ε} result which are sumarized in Table S9.

Table S9. Q_{θ} and Q_{ε} values (in Å) for the stationary points for the pseudo-rhombic $[Mn(1)F_6]^{3-}$ and pseudo-tetragonal $[Mn(2)F_6]^{3-}$ complex units, vibronic stabilization energies E_{stab} (in cm^{-1}) from ground state specific NEVPT2 calculations and the resulting K (in cm^{-1}/ $Å^2$), A_{θ}, and A_{ε} (in cm^{-1}/ Å) values, utilized in the analysis of the vibronic forces which lead to the stabilization of the two sites in K_3MnF_6.

	$[Mn(1)F_6]^{3-}$	$[Mn(2)F_6]^{3-}$
Q_{θ}	0.014	0.265
Q_{ε}	0.143	0.012
E_{stab}	−1866	−2434
K	180770	69178
A_{θ}	-2530	−18332
A_{ε}	-25850	−830

Geometry optimization/frequency calculation for the tetragonally elongated geometry

!UKS BP86 DKH DKH-DEF2-TZVPP def2/J NoFinalgrid PAL8 PrintBasis opt numfreq uno D3BJ

%cpcm epsilon 80

refrac 1.33

surfacetype vdw_gaussian

end

*xyz -3 5   # site 1 : compressed

25	0.000000000	0.000000000	0.000000000
9	1.857	0.00000	0.000000000
9	-1.857	0.0	0.000000000
9	0.0	1.857	0.000000000
9	0.0	-1.857	0.000000000
9	0.000000000	0.000000000	-2.085517223
9	0.000000000	0.000000000	2.085517223

*

Geometry optimization/frequency calculation for the tetragonally compressed geometry

!UKS BP86 DKH DKH-DEF2-TZVPP def2/J NoFinalgrid PAL8 PrintBasis opt numfreq uno D3BJ

%cpcm epsilon 80

refrac 1.33

surfacetype vdw_gaussian

end

*xyz -3 5   # site 1 : compressed

25	0.000000000	0.000000000	0.000000000
9	0.000000000	1.969218489	0.000000000
9	0.000000000	0.000000000	1.855567005
9	0.000000000	-1.969218489	0.000000000
9	0.000000000	0.000000000	-1.855567005
9	-1.969218489	0.000000000	0.000000000
9	1.969218489	0.000000000	0.000000000

*

Computational studies on the solid-state vibrational spectroscopy of $K_3[MnF_6]$

Computational details

We carried out quantum chemical vibrational spectroscopic studies on $K_3[MnF_6]$ in the solid state with the CRYSTAL17 program package.[9] We also compared $K_3[MnF_6]$ with the related compound $Na_3[MnF_6]$.[10] PBE0 hybrid density functional method and Gaussian-type basis sets were used.[11-12] The basis sets for Mn, F, K, and Na have been previously derived from the molecular Karlsruhe def2 basis sets.[13]Polarized triple-zeta-valence (TZVP) basis sets were used for Mn and F, and polarized split-valence basis set for K and Na.[14-16] The following Monkhorst-Pack-type *k*-meshes were used for sampling the reciprocal space: 2×2×2 for K_3MnF_6 and 4×4×3 for Na_3MnF_6.[17] For the evaluation of the Coulomb and exchange integrals (TOLINTEG), tight tolerance factors of 8, 8, 8, 8, and 16 were used. Both the atomic positions and lattice constants were fully optimized within the constraints imposed by the space group symmetry. The harmonic vibrational frequencies and IR intensities were obtained by using the computational schemes implemented in CRYSTAL.[18-20] The optimized structures of $K_3[MnF_6]$ and $Na_3[MnF_6]$ were confirmed to be true local minima with no imaginary frequencies. A denser 4×4×4 *k*-mesh was used for the analytical IR intensity calculations within the Coupled-Perturbed Kohn-Sham scheme. The final IR spectra were obtained by using Lorentzian peak profile with FWHM of 8 cm^{-1}.

Structural properties

We optimized the crystal structure of $K_3[MnF_6]$ in two different magnetic configurations: ferromagnetic (spin up for both Mn1 and Mn2) and antiferromagnetic (spin up for Mn1, spin down for Mn2). The crystal structure contains quasi-isolated (distorted) $[MnF_6]^{3-}$ octahedra and at the used level of theory there is no magnetic coupling between the octahedra. The FM and AFM configurations are isoenergetic and their optimized geometries are in practice identical. $Na_3[MnF_6]$ was studied only in ferromagnetic configuration. The optimized lattice parameters are in good agreement with the experimental lattice parameters of $K_3[MnF_6]$ and $Na_3[MnF_6]$, showing differences of less than 1% (Table S10).

Table S10. Optimized lattice parameters of $K_3[MnF_6]$ and $Na_3[MnF_6]$, together with a comparison to experimental lattice parameters.

Compound	Parameter	Exp. (183 K)	DFT (0 K)	Diff. (%)
$K_3[MnF_6]$	*a* (Å)	12.34	12.46	+0.9 %
	c (Å)	16.47	16.47	+0.0 %
$Na_3[MnF_6]$	*a* (Å)	5.47	5.45	–0.3 %
	b (Å)	5.68	5.64	–0.7 %
	c (Å)	8.07	8.13	+0.7 %
	β (°)	89.0	88.3	–0.8 %

Table S11 shows the Mn–F distances in the optimized structures of $K_3[MnF_6]$ and $Na_3[MnF_6]$. In the case of $K_3[MnF_6]$, the Mn2–F distances predicted by DFT are systematically 0.6–1.0% longer in comparison to the experimentally observed distances. For Mn1, the Mn1–F3 distance is almost unchanged, while the Mn1–F2 distance shortens slightly. The Mn1–F6 shows the largest change, elongating by 3.4%. The coordination octahedron around Mn1 does not, however, become similar to Mn2, where the octahedron shows one elongated Mn–F distance and two shorter, practically identical Mn–F distances. In the case of $Na_3[MnF_6]$, the axial Mn–F1 distance is elongated by 3.1% and the two equatorial Mn–F distances become practically similar.

Table S11. Mn–F distances (Å) in the optimized structures of $K_3[MnF_6]$ and $Na_3[MnF_6]$, together with a comparison to experimental distances.

Compound	Mn–F pair	Exp. (183 K)	DFT (0 K)	Diff. (%)
$K_3[MnF_6]$	Mn1–F3	1.86	1.86	+0.2 %
	Mn1–F2	1.94	1.92	–1.2 %
	Mn1–F6	2.00	2.07	+3.4 %
	Mn2–F5	2.09	2.11	+1.0 %
	Mn2–F4	1.85	1.86	+0.7 %
	Mn2–F1	1.86	1.87	+0.6 %
$Na_3[MnF_6]$	Mn–F1	2.02	2.08	+3.1 %
	Mn–F2	1.86	1.87	+0.3 %
	Mn–F3	1.90	1.88	–0.8 %

Vibrational spectroscopy

The calculated IR spectrum of $K_3[MnF_6]$ is shown in Figure S8. Only vibrational modes belonging to the irreducible representations A_u and E_u are IR active in space group $I4_1/a$. Detailed interpretation of the vibrational modes is rather complicated due to the relatively large primitive cell and due to the rather low site symmetry (–1) of the Mn1 and Mn2 atoms. The highest-energy modes are Mn–F stretching modes at about 600 cm^{-1}. This confirms the experimental assignment that modes above 600 cm^{-1} likely arise from unreacted starting materials. The modes between 350 and 600 cm^{-1} are all various Mn–F stretching modes (details in Table S12). The Mn–F stretching modes at around 550 cm^{-1}, clearly visible in the experimental IR spectrum, arise from a complex mixing of both Mn1–F and Mn2–F stretching modes. The mode at around 510 cm^{-1}, possibly visible as a shoulder in the experimental IR spectrum, mainly arises from Mn1–F stretching modes. The experimental IR spectrum ends at about 400 cm^{-1}, but the mode partially shown at that point could be Mn1–F6 stretching mode seen at 393 cm^{-1} in the calculated spectrum (the longest Mn1–F distance). The stretching vibration for the Mn2–F5 distance occurs at 353 cm^{-1} (the longest Mn2–F distance).

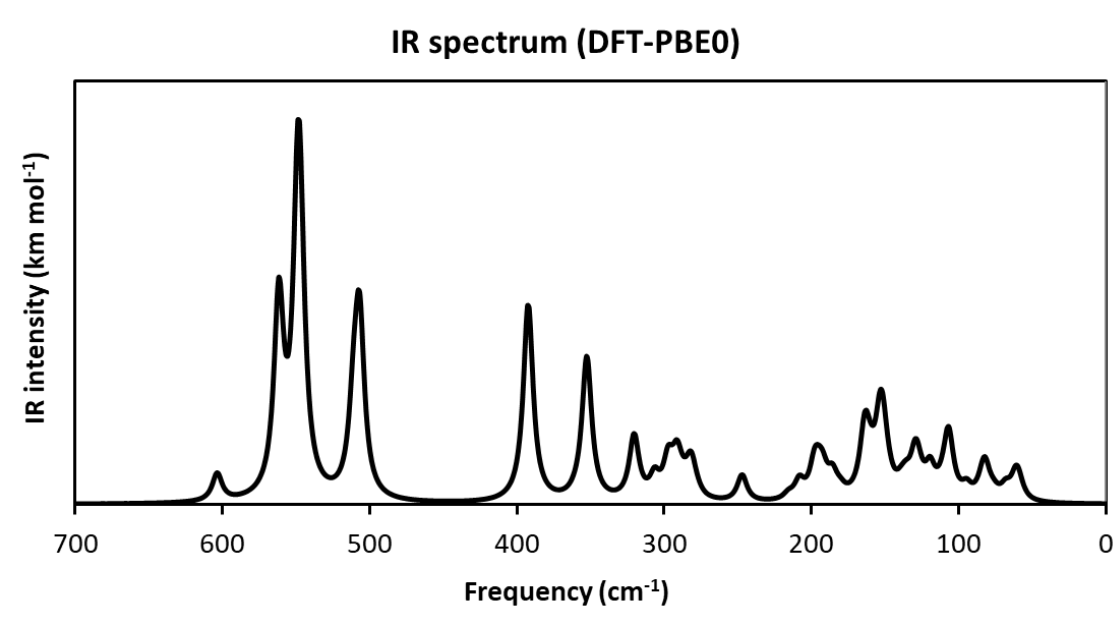

Figure S8. Calculated IR spectrum of $K_3[MnF_6]$

Table S12. IR active vibrational modes in $K_3[MnF_6]$. Only vibrational modes belonging to the irreducible representations A_u and E_u are IR active (space group $I4_1/a$). See text for more details.

Mode	Freq. (cm-1)	Irrep	IR intensity (km mol-1)	Comment
8	59	Au	98	
9-10	61	Eu	95	
11	62	Au	73	
13-14	68	Eu	87	
19	73	Au	5	
23-24	77	Eu	44	
27	80	Au	3	
29-30	82	Eu	227	
34-35	84	Eu	79	
43-44	95	Eu	60	
46	95	Au	25	
52	107	Au	140	
53-54	107	Eu	355	
58-59	111	Eu	44	
62	115	Au	8	
63	120	Au	201	
70-71	127	Eu	50	
72	128	Au	67	
73-74	130	Eu	267	
76	132	Au	5	
80-81	136	Eu	103	
84	139	Au	61	
91-92	148	Eu	46	
95	152	Au	371	
96-97	154	Eu	392	
102-103	160	Eu	110	
105	163	Au	339	
107-108	165	Eu	177	
114	170	Au	1	
119	180	Au	17	
120	181	Au	19	
121-122	181	Eu	16	
124-125	186	Eu	157	
128	193	Au	161	
131-132	195	Eu	116	
133-134	198	Eu	200	
135	199	Au	29	
137-138	208	Eu	134	
142	216	Au	42	
149	237	Au	0	
154-155	247	Eu	198	
162-163	277	Eu	18	
167	281	Au	191	
168-169	283	Eu	118	
175	288	Au	47	
177-178	292	Eu	283	Mn2–F bending (mainly)
180	294	Au	10	
184	297	Au	20	
185-186	298	Eu	246	Mn1–F bending (mainly)
189	307	Au	0	
190-191	307	Eu	155	Mn2–F bending (mainly)
194-195	321	Eu	474	Mn1–F bending (mainly)
198	323	Au	1	
202-203	353	Eu	1070	Mn2–F5 stretching (mainly)
204	361	Au	10	
210-211	393	Eu	1472	Mn1–F6 stretching (mainly)
216	409	Au	0	
217	507	Au	1264	Mn1–F stretching (mainly)
218-219	511	Eu	545	Mn1–F stretching (mainly)
229-230	547	Eu	812	Mn1–F and Mn2–F stretching
231	549	Au	2044	Mn1–F and Mn2–F stretching
244	558	Au	2	
234-235	562	Eu	1442	Mn1–F and Mn2–F stretching
238-239	604	Eu	204	Mn1–F and Mn2–F stretching
240	609	Au	1	

The experimental Raman spectrum only shows intensive modes below 100 cm^{-1}. Based on the calculated vibrational properties, the Raman-active symmetric Mn–F stretching modes would be expected at around 540 cm^{-1} (Mn2) and 520 cm^{-1} (Mn1).

Optimized structures in CIF format

Note that the CIFs below have been standardized by FINDSYM (https://stokes.byu.edu/iso/findsym.php) after the geometry optimization. The calculations have been run starting from the experimental CIF (Mn1 in position 8d) and the computational discussion above also refers to that situation.

```
data_K3MnF6_DFT-PBE0_TZVP
_audit_creation_method FINDSYM

_cell_length_a    12.4590637984
_cell_length_b    12.4590637984
_cell_length_c    16.4717295232
_cell_angle_alpha 90.0000000000
_cell_angle_beta  90.0000000000
_cell_angle_gamma 90.0000000000

_symmetry_space_group_name_H-M "I 41/a (origin choice 2)"
_symmetry_Int_Tables_number 88
_space_group.reference_setting '088:-I 4ad'
_space_group.transform_Pp_abc a,b,c;0,0,0

loop_
_space_group_symop_id
_space_group_symop_operation_xyz
1 x,y,z
2 -x,-y+1/2,z
3 -y+3/4,x+1/4,z+1/4
4 y+1/4,-x+1/4,z+1/4
5 -x,-y,-z
6 x,y+1/2,-z
7 y+1/4,-x+3/4,-z+3/4
8 -y+3/4,x+3/4,-z+3/4
9 x+1/2,y+1/2,z+1/2
10 -x+1/2,-y,z+1/2
11 -y+1/4,x+3/4,z+3/4
12 y+3/4,-x+3/4,z+3/4
13 -x+1/2,-y+1/2,-z+1/2
14 x+1/2,y,-z+1/2
15 y+3/4,-x+1/4,-z+1/4
16 -y+1/4,x+1/4,-z+1/4

loop_
_atom_site_label
_atom_site_type_symbol
_atom_site_symmetry_multiplicity
_atom_site_Wyckoff_label
_atom_site_fract_x
_atom_site_fract_y
_atom_site_fract_z
_atom_site_occupancy
Mn1 Mn   8 c 0.00000 0.00000 0.00000 1.00000
Mn2 Mn   8 d 0.00000 0.00000 0.50000 1.00000
K1  K   16 f 0.47622 0.01747 0.27459 1.00000
K2  K   16 f 0.79494 0.50639 0.36066 1.00000
K3  K    8 e 0.00000 0.25000 0.86726 1.00000
K4  K    4 a 0.00000 0.25000 0.12500 1.00000
K5  K    4 b 0.00000 0.25000 0.62500 1.00000
F1  F   16 f 0.76277 0.73491 0.36280 1.00000
F2  F   16 f 0.31913 0.16619 0.33241 1.00000
F3  F   16 f 0.30386 0.15578 0.17255 1.00000
F4  F   16 f 0.89168 0.60304 0.49584 1.00000
F5  F   16 f 0.88414 0.37805 0.48662 1.00000
F6  F   16 f 0.88772 0.34070 0.26391 1.00000

data_Na3MnF6_DFT-PBE0_TZVP
_audit_creation_method FINDSYM

_cell_length_a    5.4535879600
_cell_length_b    5.6447098600
```

```
_cell_length_c    9.6508643531
_cell_angle_alpha 90.0000000000
_cell_angle_beta  122.6752134498
_cell_angle_gamma 90.0000000000

_symmetry_space_group_name_H-M "P 1 21/c 1"
_symmetry_Int_Tables_number 14
_space_group.reference_setting '014:-P 2ybc'
_space_group.transform_Pp_abc a,b,c;0,0,0

loop_
_space_group_symop_id
_space_group_symop_operation_xyz
1 x,y,z
2 -x,y+1/2,-z+1/2
3 -x,-y,-z
4 x,-y+1/2,z+1/2

loop_
_atom_site_label
_atom_site_type_symbol
_atom_site_symmetry_multiplicity
_atom_site_Wyckoff_label
_atom_site_fract_x
_atom_site_fract_y
_atom_site_fract_z
_atom_site_occupancy
Mn1 Mn   2 a 0.00000 0.00000 0.00000 1.00000
Na1 Na   2 d 0.50000 0.00000 0.50000 1.00000
Na2 Na   4 e 0.75919 0.44552 0.75089 1.00000
F1  F    4 e 0.35624 0.56379 0.73661 1.00000
F2  F    4 e 0.77760 0.67249 0.55883 1.00000
F3  F    4 e 0.09339 0.77932 0.43162 1.00000
```

References

[1] G. I. Finch, S. Fordham, *Proc. Phys. Soc.* **1936,** *48*, 85-94.
[2] F. Schrötter, B. G. Müller, *Z. Anorg. Allg. Chem.* **1993,** *619*, 1426-1430.
[3] R. D. Peacock, D. W. A. Sharp, *J. Chem. Soc.* **1959**, 2762-2767.
[4] M. Mylarappa, V. V. Lakshmi, K. R. V. Mahesh, H. P. Nagaswarupa, N. Raghavendra, *IOP Conf. Ser.: Mater. Sci. Eng.* **2016,** *149*, 012178.
[5] J. A. A. Ketelaar, W. Vedder, *J. Chem. Phys.* **1951,** *19*, 654-654.
[6] I. B. Bersuker, *The Jahn-Teller Effect and Vibronic Interactions in Modern Chemistry*. Plenum Press, New York and London,
[7] J. A. Aramburu, García-Lastra, P. García-Fernández, M. T. Barriuso, M. Moreno, *Inorg. Chem.* **2013,** *52*, 6923-6933.
[8] J. A. Aramburu, García-Lastra, P. García-Fernández, M. Moreno, *J. Phys. Chem. C* **2017,** *121*, 5215-5224.
[9] R. Dovesi, A. Erba, R. Orlando, C. M. Zicovich-Wilson, B. Civalleri, L. Maschio, M. Rérat, S. Casassa, J. Baima, S. Salustro, B. Kirtman, *Wiley Interdiscip. Rev: Comput Mol. Sci.* **2018,** *8*, 1-36.
[10] U. Englich, W. Massa, A. Tressaud, *Acta Cryst. Sect. C* **1992,** *48*, 6-8.
[11] J. Perdew, K. Burke, M. Ernzerhof, *Phys. Rev. Lett.* **1996,** *77*, 3865-3868.
[12] C. Adamo, V. Barone, *Chem. Phys.* **1999,** *110*, 6158-6170.
[13] F. Weigend, R. Ahlrichs, *Phys. Chem. Chem. Phys.* **2005,** *7*, 3297-3305.
[14] J. Linnera, A. J. Karttunen, *Phys. Rev. B.* **2019,** *100*, 144307.
[15] A. J. Karttunen, T. Tynell, M. Karppinen, *J. Phys. Chem. C* **2015,** *119*, 13105-13114.
[16] R. E. Stene, B. Scheibe, A. J. Karttunen, W. Petry, F. Kraus, *Eur. J. Inorg. Chem.* **2019,** *2019*, 3672-3682.
[17] H. J. Monkhorst, J. D. Pack, *Phys. Rev. B.* **1976,** *13*, 5188-5192.
[18] F. Pascale, C. M. Zicovich-Wilson, F. L. Gejo, B. Civalleri, R. Orlando, R. Dovesi, *Comput. Chem.* **2004,** *25*, 888-897.
[19] C. Zicovich-Wilson, F. Pascale, C. Roetti, V. Saunders, R. Orlando, R. Dovesi, *Comput. Chem.* **2004,** *25*, 1873-1881.
[20] L. Maschio, B. Kirtman, R. Orlando, M. Rèrat, *J. Chem. Phys.* **2012,** *137*, 204113.